Chapter 5

Reversible metal ion (Li^+, Na^+, Mg^{2+}, Al^{3+}) insertion in $MoTe_2$ for rechargeable aqueous battery

Nandi, S., Yan, Y., Yuan, X., Wang, C., He, X., Li, Y., and Das, S. K. (*Phys. Chem. Chem. Phys*., revision submitted 2023)

Molybdenum ditelluride ($MoTe_2$) for reversible metal ion (Li^+, Na^+, Mg^{2+}, Al^{3+}) insertion

5.1 Introduction

Recently, 2D transition metal dichalcogenides (TMDCs) have emerged as a promising electrode material for electrochemical energy storage due to their excellent physicochemical properties and atomic arrangement [1-4]. In general, TMDCs are layered materials where two chalcogen atomic layers (i.e., X-M-X, where M= transitional metal and X= chalcogen atom) are held together by a weak van der Waal's force. This unique 2D structure facilitates facile guest ion insertion [1-4]. An example of TMDCs is molybdenum ditelluride ($MoTe_2$) with an interlayer spacing of 0.69 nm. Unlike other TMDCs such as MoS_2, $MoSe_2$, VS_2, WS_2, etc., $MoTe_2$ has not received much attention in the area of energy storage [5-8]. In addition, TMDCs shows low conductivity, poor stability, electrode pulverization, which are not feasible for battery applications. There are only a few battery-related reports of $MoTe_2$ [9-11]. For example, Cho et al. reported that $MoTe_2$ microspheres with a core-shell structure delivered a Na^+ ion storage capacity of 286 mAg^{-1} over 200 cycles at a current rate of 1 Ag^{-1} [9]. Ma et al. fabricated $MoTe_2$ nanosheets with few-layer graphene for Li^+ ion batteries, which shows a stable discharge capacity of 574 $mAhg^{-1}$ at a current density of 0.5 Ag^{-1} over 400 cycles [10]. Similarly, Panda et al. demonstrated the electrochemical performance of $MoTe_2$ as an anode material for Li^+ ion batteries. The anode could retain a reversible discharge capacity of 291 $mAhg^{-1}$ after 260 cycles at 1 Ag^{-1} [11]. All these studies have been performed in non-aqueous electrolytes. There are no reports on insertion of these ions in aqueous electrolytes. In addition, there is no report altogether on the Al^{3+} ion electrochemistry of $MoTe_2$ for rechargeable Al-metal/Al-ion battery. Therefore, in this chapter, the electrochemical behavior of $MoTe_2$ in aqueous systems is discussed using various metal ions such as Li^+, Na^+, Mg^{2+}, and Al^{3+} ion aqueous electrolytes with a special focus on the Al^{3+} ion storage.

5.2 Experimental Section

5.2.1 Materials

Telluride powder (Te, Sigma Aldrich), Sodium borohydride ($NaBH_4$, Sigma Aldrich), Sodium molybdate dihydrate ($Na_2MoO_4.2H_2O$, Sigma Aldrich), Ethanol and Distilled water.

5.2.2 Synthesis

$MoTe_2$ powder was prepared via a facile one-pot hydrothermal process adapted from a previous report [12]. In brief, 766 mg of tellurium metal (Te) powder and 700 mg of sodium borohydride ($NaBH_4$) were added to 5 ml of DI water in an ice bath. After 30 min, a clear Te precursor was obtained. Then, 726 mg of sodium molybdate dihydrate ($Na_2MoO_4.2H_2O$) was added to 30 ml of DI water and stir for 10 min. Then, the as-formed mixture was added to the Te precursor and stirred for another 30 min, followed by transfer of the mixture to a Teflon-lined stainless autoclave (50 ml) and heated at 200 ^oC for 48 h. After cooling down to room temperature, the precipitates were collected, washed with deionized water and ethanol for three times and dried at 60 ^oC for 12 h.

5.2.3 Characterization

The crystal structure and morphology were characterized by X-ray diffraction (XRD, Rigaku Miniflex II diffractometer with Cu Kα radiation operated at 30 kV and 15 mA), Field emission electron microscopy (FESEM, ZEISS Supra 40V), and Transmission electron microscopy (TEM, JEOL-2010 F). The surface chemical compositions of the samples were analyzed by X-ray photoelectron spectroscopy (XPS, AXIS Ultra DLD system).

5.2.4 Electrochemical analysis:

Electrode slurry was prepared by mixing the active material ($MoTe_2$) with PVDF in a weight ratio of 80:20 using N-methyl-2-pyrrolidone solvent. The slurry was drop cast on a carbon cloth (14mm in diameter, Fuel cell store, USA, ELAT hydrophilic, Product code: 1591002) and dried at 60 ^oC for 12 h.

Cyclic voltammetry (CV) and galvanostatic discharge/charge experiments were conducted in a conventional three-electrode electrochemical glass cell where a Pt electrode and Ag/AgCl electrode were used as the counter and reference electrodes, respectively. The discharge/charge and CV experiments were performed in a voltage range of -0.7 to 0.8 V (vs. Ag/AgCl). Electrochemical impedance spectra (EIS) were recorded in frequency range of 1 mHz-200 kHz at 10 mV signal amplitude. All the electrochemical tests were performed at room temperature (25 ^oC)

5.3 Results and Discussion

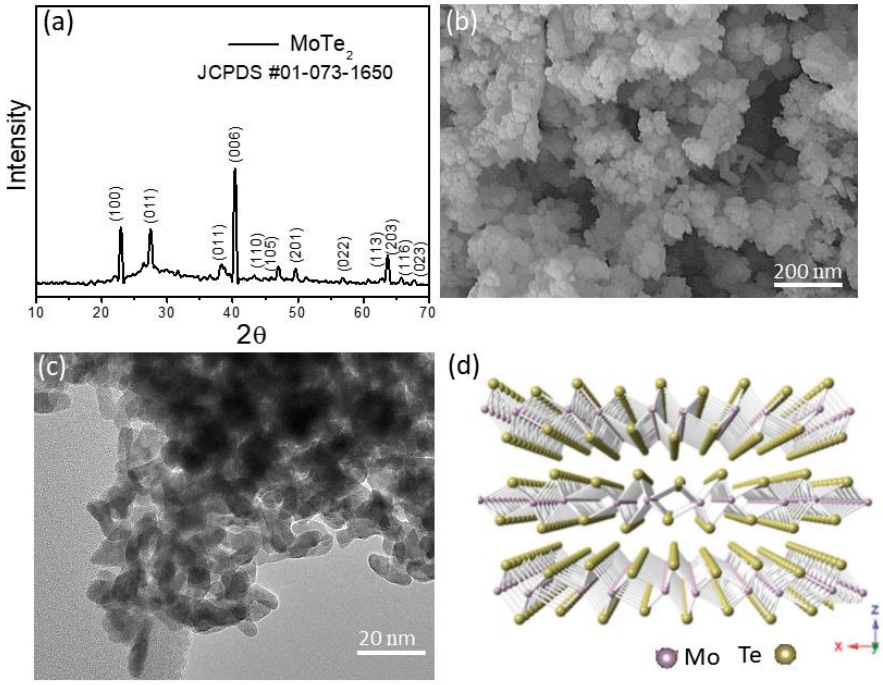

Figure 5.1 (a) XRD pattern, (b) FESEM and (c) TEM images of $MoTe_2$. (d) Crystal structure of $MoTe_2$. Reproduced with permission from ref. [10], copyright 2018 Wiley Journal.

Figure 5.1a shows the X-ray diffraction (XRD) pattern of the as-prepared $MoTe_2$. The material can be well indexed to the hexagonal crystal phase of $MoTe_2$ with a space group $P6_3/mmc$ (JCPDS no. 01-073-1650), demonstrating the successful synthesis of the material. Field emission scanning electron microscopy (FESEM) images of $MoTe_2$ showed the formation of grain-like nanoparticles (Figure 5.1b). It is also supported by the TEM image (Figure 5.1c). The crystal structure of $MoTe_2$ is also shown in Figure 5.1d.

To study the electrochemical activity of $MoTe_2$, cyclic voltammetry and galvanostatic discharge/charge experiments were carried out in different electrolytes in the voltage window of -0.7 V to 0.8 V (vs Ag/AgCl). Figure 5.2a shows the CV profile in 1 M $AlCl_3$ aqueous electrolyte at a scan rate of 2.5 mVs^{-1}. It indicates a pair of highly reversible prominent redox peaks. The cathodic (A) and anodic (B) peaks are located at -0.28 V and 0.38 V respectively. The CV profiles are nearly superimposing each other, except a slight shift of peak A in the initial cathodic cycle, signifying a stable electrochemical activity. Further, CV experiments were also conducted in 1 M LiCl, 1 M NaCl and 1 M $MgCl_2$ aqueous electrolytes at a similar

scan rate. As shown in Figure 5.2b, similar electrochemical behavior could be observed in 1 M LiCl electrolyte. However, the redox peaks are located at different positions (cathodic peak at -0.49 V and anodic peak at 0.4 V). On the other hand, in case of 1 M NaCl electrolyte, two cathodic peaks (labeled as P, Q) at -0.47 V and -0.22 V and one anodic peak (labeled as R) at 0.4 V could be noticed (Figure 5.2c). Again, in the case of 1 M $MgCl_2$ electrolyte, $MoTe_2$ exhibits two closely spaced cathodic peaks (labeled as S and T) at -0.55 V and -0.42 V and one minor peak (labeled as U) at -0.19 V. On the anodic side, two anodic peaks (labeled as Y and Z) at 0.1 V and 0.46 V are observed (Figure 5.2d). It is to be noted here that the redox peak intensities gradually decrease with subsequent cycles for all these aqueous electrolytes except 1 M $AlCl_3$ aqueous electrolyte, demonstrating irreversibility to a certain degree.

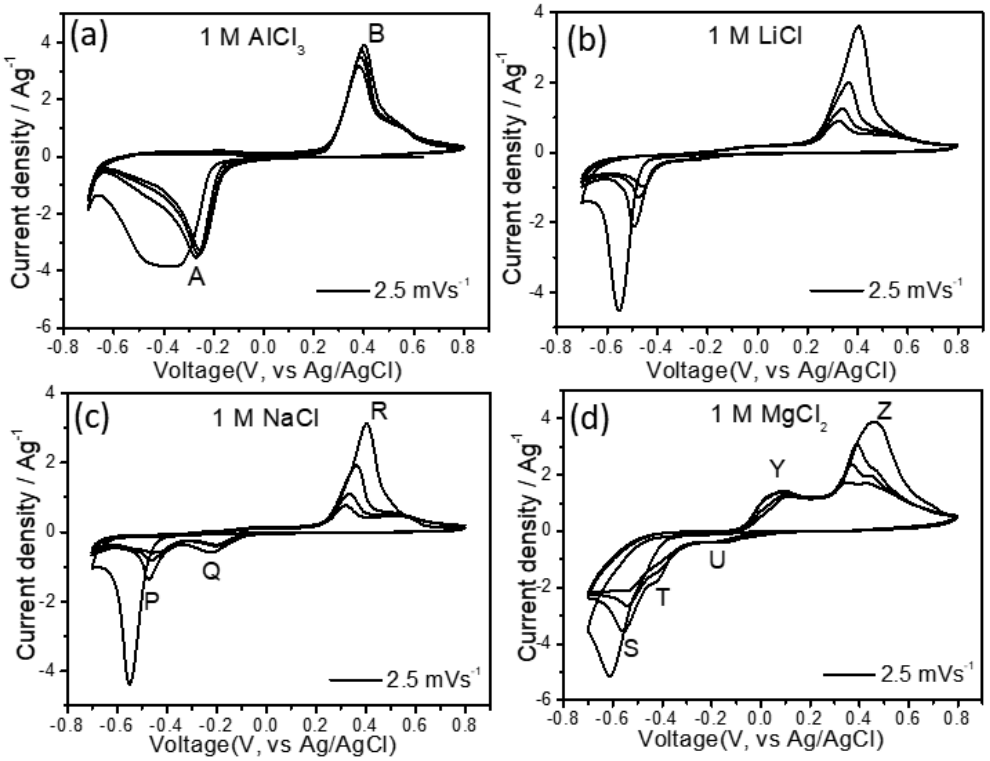

Figure 5.2 CV curves of $MoTe_2$ at a scan rate of 2.5 mVs^{-1} in (a) 1 M $AlCl_3$, (b) 1 M LiCl, (c) 1 M NaCl, and (d) 1 M $MgCl_2$ aqueous electrolytes respectively.

The outcome of CV measurements was further corroborated with galvanostatic measurement to evaluate the ion storage capacities of $MoTe_2$. Figure 5.3a shows the charge/discharge profiles in 1 M $AlCl_3$ aqueous electrolyte in the voltage range of -0.7 V to 0.8 V (vs. Ag/AgCl) at a specific current rate of 1 Ag^{-1}. There exists a long

discharge potential plateau at -0.12 V and a charge plateau at 0.28 V in all the measured cycles, which is fairly consistent with the CV curves (Figure 5.2a). An initial discharge and charge capacities of 420 $mAhg^{-1}$ and 270 $mAhg^{-1}$ were estimated. These discharge/charge profiles are however different from the rest of the investigated electrolytes. For example, as could be seen in Figure 5.3b, there are two short discharge plateaus at -0.21 V and -0.4 V in case of LiCl electrolyte. The same plateaus are also observed for NaCl electrolyte except a slight change in one of the discharge plateaus which is at -0.16 V instead of -0.21 V (Figure 5.3c). The charge plateau is at the same potential (0.28 V) for both cases. For the $MgCl_2$ electrolyte, there is a long discharge plateau at -0.4 V and a very short discharge plateau at -0.13 V with subsequent two charge plateaus at 0.03 V and 0.28 V (Figure 5.3d). In all cases, the initial discharge profile is slightly different from the rest of the cycles. All these features are completely matching with the corresponding CV profiles. In terms of ion storage capacity and capacity retention, from the plot of variation of discharge capacities with cycle number as shown in Figure 5.3e, it is seen that $MoTe_2$ exhibits not only highest Al^{3+} ion storage capacity but also shows best cycling stability. It is estimated that $MoTe_2$ delivers a discharge capacity of 100 $mAhg^{-1}$ over 250 cycles in 1 M $AlCl_3$ aqueous electrolyte. Even at a higher current rate of 5 Ag^{-1}, a discharge capacity of 50 $mAhg^{-1}$ over 2000 cycles could be delivered (Figure 5.4). In contrast, the discharge capacities decrease gradually with increase in cycle number in all the other electrolytes (Figure 5.3e). In fact, the capacities reached to almost zero after a few cycles in 1 M LiCl and 1 M NaCl electrolytes. In addition, the polarization is lowest in the case of Al^{3+} ion which is around 0.17 V. The better electrochemical performance in case of $AlCl_3$ electrolyte may be attributed to the lower charge-transfer resistance and this is supported by electrochemical impedance spectroscopy analysis. In Figure 5.3f, it could be seen that the charge-transfer resistance is smaller for Al^{3+} ion than that of Mg^{2+}, Na^+ and Li^+ ions.

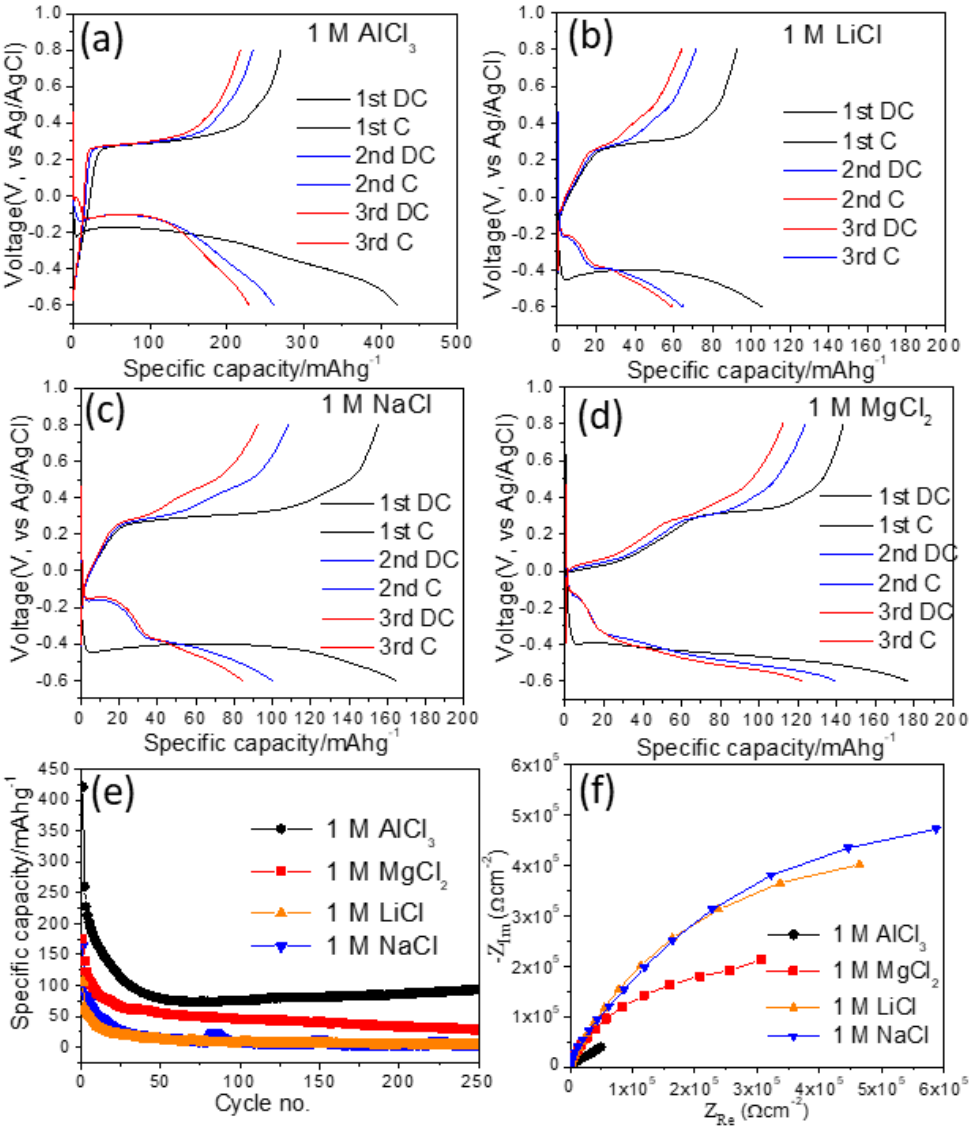

Figure 5.3 (a) Galvanostatic discharge/charge curves of $MoTe_2$ in (a) 1 M $AlCl_3$, (b) 1 M LiCl, (c) 1 M NaCl, and (d) 1 M $MgCl_2$ aqueous electrolytes, (e) Variation of discharge capacities with cycle number. The current density is 1 Ag^{-1}. (f) Electrochemical impedance in different electrolytes.

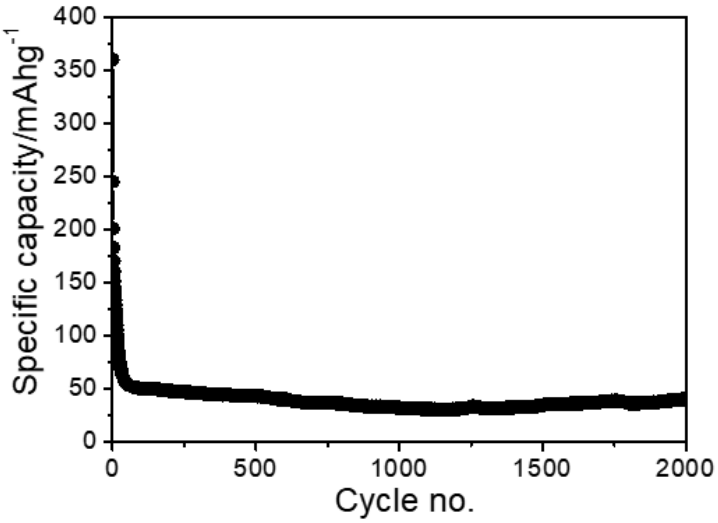

Figure 5.4 Variation of discharge capacities with cycle in 1 M $AlCl_3$ aqueous electrolyte at a current density of 5 Ag^{-1}.

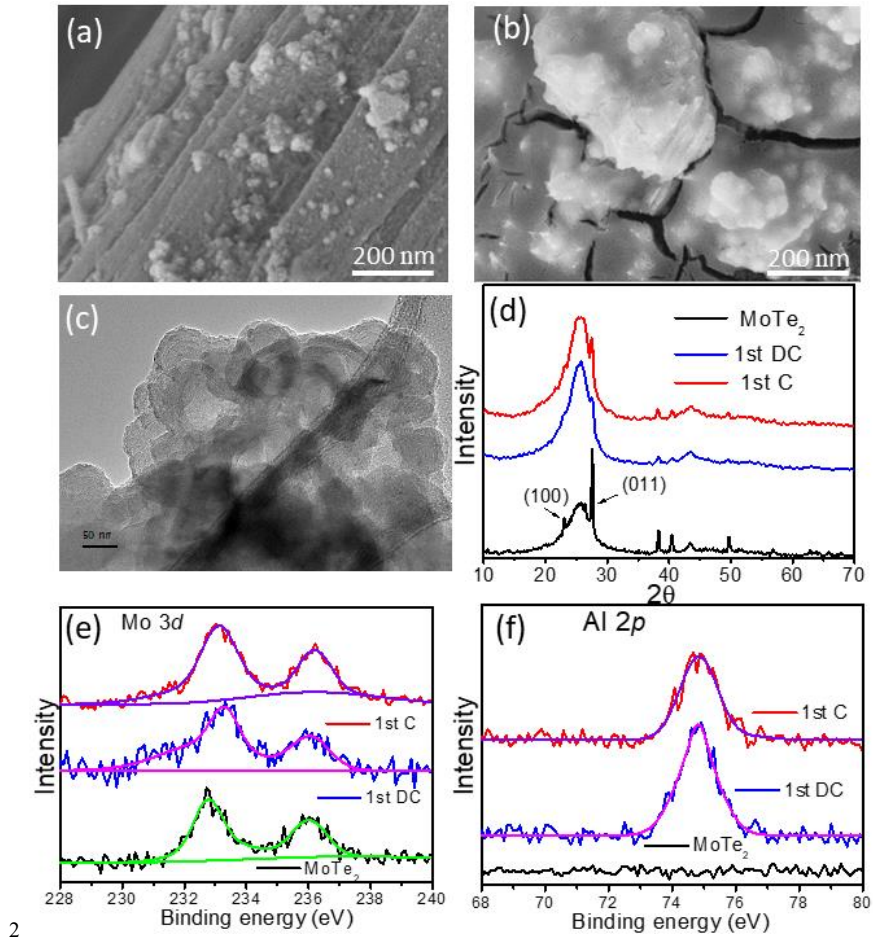

2

Figure 5.5 Ex-situ-FESEM images of $MoTe_2$ (a) before and (b) after 1st discharge, (c) ex-situ TEM image after 1st discharge state, (d) Ex-situ XRD patterns of $MoTe_2$ before and after 1st discharge and 1st charge state, and Ex-situ XPS spectra of (e) Mo 3*d*, and (f) Al 2*p* before and after 1st discharge and 1st charge state respectively.

To understand the electrochemical mechanism of Al^{3+} ion insertion in $MoTe_2$, the discharged and charged state electrodes were analyzed using electron microscopy, X-ray photoelectron spectroscopy (XPS) and XRD techniques. Ex-situ FESEM image of $MoTe_2$ electrode before and after 1st discharge (Figure 5.5a, b) shows a thick conglomeration of materials accompanied with cracks in it. A similar scenario was seen in case of charged electrode also (Figure 5.6). The ex-situ TEM image (Figure 5.5c) also indicates a change in the morphology of $MoTe_2$ compared to Figure 5.1c. Ex-situ XRD patterns of $MoTe_2$ electrodes are shown in Figure 5.5d. It could be observed that $MoTe_2$ electrode almost loses its crystallinity after 1st discharge as evident from the diminished peak intensities for the typical (100) and (011) peaks of $MoTe_2$ at $2\theta = 23.07^o$ and 27.06^o. However, there are no appearances of additional peaks also. The XRD pattern of the charged electrode is almost identical to the discharged state electrode. This indicates that there is structural irreversibility of $MoTe_2$ after the electrochemical reaction. In order to further verify this event, ex-situ XRD experiments were performed with $MoTe_2$ electrodes after initial discharge and charge in 1 M NaCl aqueous electrolyte (Figure 5.7). These XRD patterns possess two additional peaks at $2\theta = 31.9^o$ and 45.5^o, which could be indexed to the pristine Mo phase (JCPDS no. 01-1208). Figure 5.5 (e) and Figure 5.8 show the ex-situ XPS spectra of Mo 3*d* and Te 3*d* after the 1st discharge and 1st charge states. The Mo 3*d* spectrum showed two prominent peaks at 232.7 eV and 235.9 eV, corresponding to Mo $3d_{3/2}$ and Mo $3d_{5/2}$, respectively [5-6]. After the 1st discharge, the Mo 3*d* peaks shifted to higher binding energy, indicating reduction of $MoTe_2$ to Mo upon insertion of Al^{3+} ion. However, after the 1st charge Mo 3*d* doesn't return to its initial position similar to the XRD patterns. The strong peak of Al 2*p* at 74.6 eV during 1st discharge could be seen in both discharge and charge processes [13]. On the other hand, no peak shift was observed in the Te 3d spectra during the discharge/charge process, indicating the valence states of Te remains stable during the electrochemical process (Figure 5.8). CV experiment was also performed at different scan rates in 1 M $AlCl_3$ aqueous electrolyte as shown in Figure 5.9 and it revealed that the peak current responses (I) for both the cathodic and anodic redox peaks do not follow any relationship with scan rates (γ) according to the equation $I = k\gamma^{0.5}$ (k is a constant), which hints for a non-diffusive ion insertion/extraction process [14]. Based on these analyses, the following conversion type electrochemical mechanism is plausible: (i)

$3MoTe_2 + 4Al^{3+} + 12e^- \rightarrow 3Mo + 2Al_2Te_3$. It is to be noted here that the XRD peaks of Al_2Te_3 at $2\theta = 23.1^o$, 27.43^o, 40.45^o and 49.6^o superimpose with $MoTe_2$ phase [15]. Based on the electrochemical reaction, the theoretical capacity is estimated to be 890 $mAhg^{-1}$.

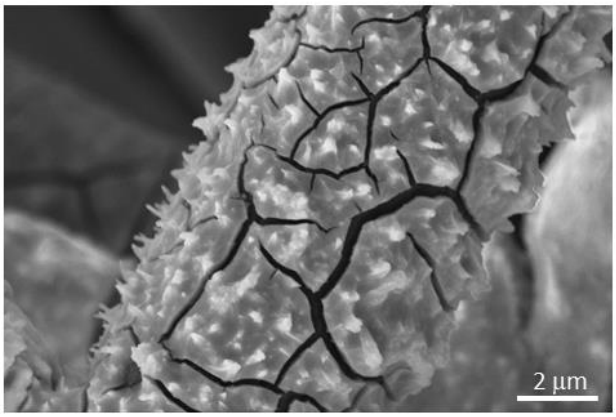

Figure 5.6 Ex-situ FESEM image of $MoTe_2$ after the 1st charge state.

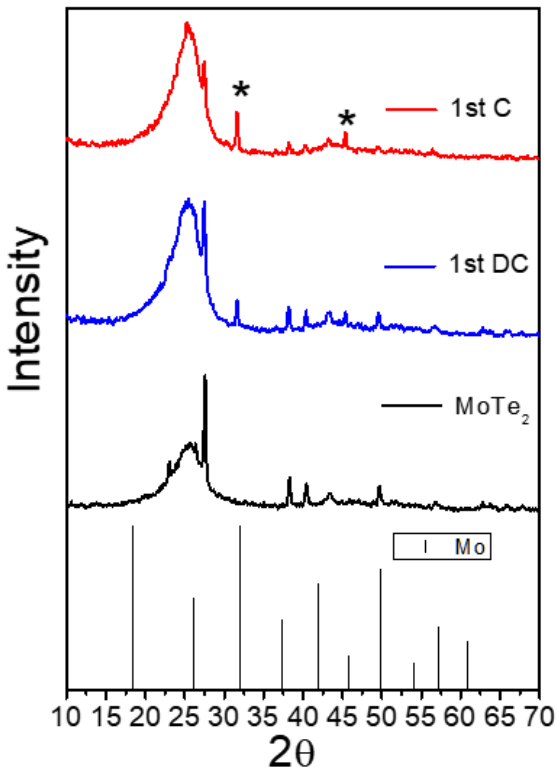

Figure 5.7 Ex-situ XRD patterns of $MoTe_2$ before and after 1st discharge/ 1st charge state in 1 M NaCl aqueous electrolyte.

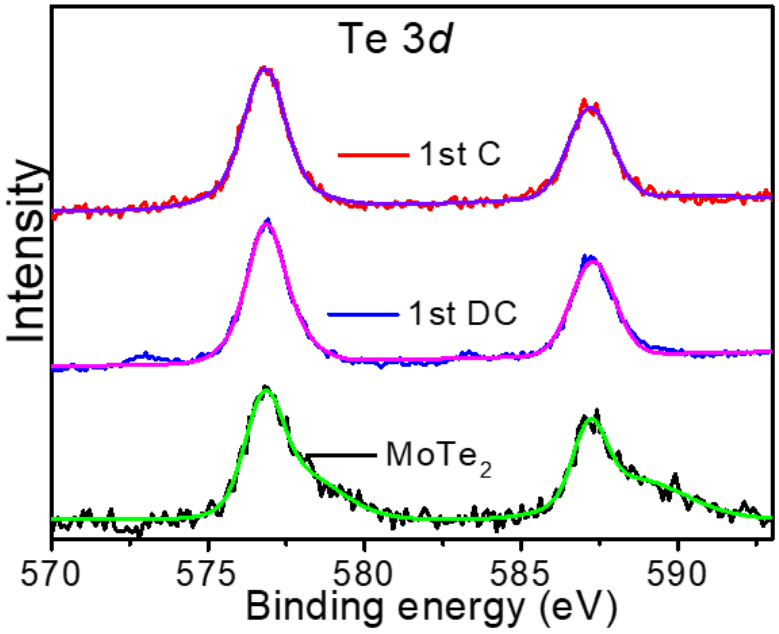

Figure 5.8 Ex-situ XPS spectra of Te 3*d* before and after 1st discharge/ 1st charge state respectively.

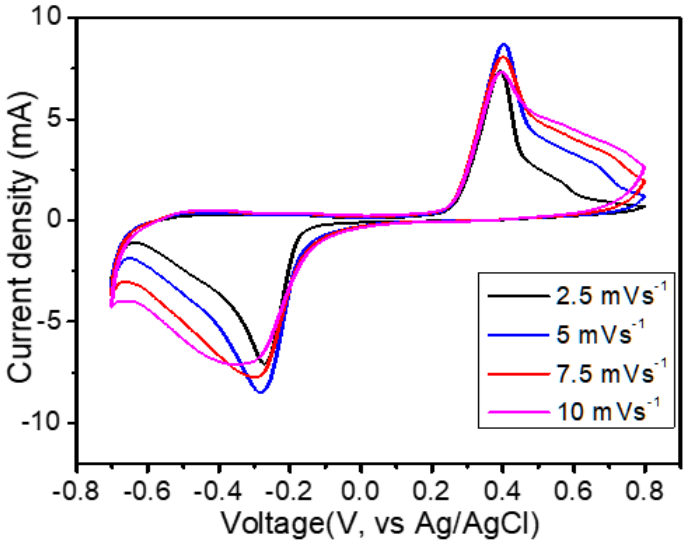

Figure 5.9 CV curves of $MoTe_2$ at different scan rates in 1 M $AlCl_3$ aqueous electrolyte.

5.4 Conclusion

In summary, this chapter demonstrated the electrochemical behavior of $MoTe_2$ in Li^+, Na^+, Mg^{2+}, Al^{3+} ion conducting aqueous electrolytes. It was found that $MoTe_2$ exhibits superior electrochemical performance in 1 M $AlCl_3$ aqueous electrolyte with a discharge specific capacity of 100 $mAhg^{-1}$ after 250

cycles at 1 Ag^{-1} and excellent long term cycling performance (50 $mAhg^{-1}$ over 2000 cycles at a current density of 5 Ag^{-1}). In contrast, the discharge capacities observed in 1 M LiCl and 1 M NaCl electrolytes reached to almost zero after a few cycles. It is highlighted that there may be a possibility of crystal phase transition of $MoTe_2$ to aluminum telluride phase due to Al^{3+} ion intercalation. The polarization is lowest in the case of Al^{3+} ion which is around 0.17 V.

5.5 References

[1] Choudhary, N., Islam, Md. A., Kim, J. H., Ko, T.J., Schropp. A., Hurtado, L., Weitzman, D., Zhai, L., and Jung, Y. Two-dimensional transition metal dichalcogenide hybrid materials for energy applications. *Nano. Today*, 19:16-40. 2018.

[2] Yang, E., Ji, H., and Jung, Y. Two-dimensional transition metal dichalcogenide monolayers as promising sodium ion battery anodes. *J. Phys. Chem. C,* 119:26374, 2015.

[3] Lin, L., Lei, W., Zhang, S., Liu, Y., and Wallace, G. G. Two-dimensional transition metal dichalcogenides in supercapacitors and secondary batteries. *Energy Stor. Mater.*, 19:408-423, 2019.

[4] Soares, D. M., Mukherjee, S., and Singh, G. TMDs beyond MoS_2 for electrochemical energy storage. *Chem. A Eur. J.*, 26: 6320-6341, 2020.

[5] Li, Z., Niu, B., Liu, J., Li, J., and Kang, F. Rechargeable aluminum-ion battery based on MoS_2 microsphere cathode. *ACS Appl. Mater. Interfaces* 10: 9451–9459, 2018.

[6] Zhou, Q., Wang, D., Lian, Y., Hou, S., Ban C., Wang, Z., Zhao, J., and Zhang, H. Rechargeable aluminum-ion battery with sheet-like $MoSe_2$@C nanocomposites cathode. *Electrochim. Acta* 354: 136677, 2020.

[7] Wu, L., Sun, R., Xiong, F., Pei, C., Han, K., Peng, C., Fan, Y., Yang, W., An, Q., and Mai, L., A rechargeable aluminum-ion battery based on a VS_2 nanosheet cathode. *Phys. Chem. Chem. Phys.*, 20: 22563-22568, 2018.

[8] Latha, M., and Rani, J. V. WS_2/Graphene composite as cathode for rechargeable aluminum-dual ion battery. *J. Electrochem. Soc.*, 167: 070501, 2020.

[9] Cho, J. S., Ju, H. S., Lee, J.-K., and Kang, Y. C. Carbon/two-dimensional $MoTe_2$ core/shell-structured microspheres as an anode material for Na-ion batteries. *Nano.*, 9: 1942-1950, 2017.

[10] Ma, N., Jiang, X.-Y., Zhang, L., Wang, X.-S., Cao, Y.-L., and Zhang, X.-Z. Novel 2D Layered molybdenum ditelluride encapsulated in few-layer graphene as high-performance anode for lithium-ion batteries. *Small*, 14:1703680, 2018.

[11] Panda, M. R., Gangwar, R., Muthuraj, D., Sau, S., Pandey, D., Banerjee, A. Chakrabarti, A., Sagdeo, A., Weyland, M., Majumder, M., Bao, Q., and Mitra, S. High performance lithium-ion batteries using layered 2H-$MoTe_2$ as anode. *Small*, 16: 2002669, 2020.

[12] Ding, L., Wei, J., Qiu, Y., Wang, Y., Wen, Z., Qian, J., Hao, N., Ding, C., Li, Y., and Wang, K., One-step hydrothermal synthesis of telluride molybdenum/reduced graphene oxide with Schottky barrier for fabricating label-free photoelectrochemical profenofos aptasensor. *Chem. Eng. J.*, 407: 127213, 2021.

[13] Wu, C., Gu, S., Zhang, Q., Bai, Y., Li, M., Yuan, Y., Wang, H., Liu, X., Yuan, Y., Zhu, N., Wu, F., Li, H., Gu, L., and Lu, J., Electrochemically activated spinel manganese oxide for rechargeable aqueous aluminum battery. *Nat. Commun.*, 10:73, 2019.

[14] Wang, J., Polleux, J., Lim, J., and Dunn, B. Pseudocapacitive contributions to electrochemical energy storage in TiO_2 (anatase) nanoparticles. *J. Phys. Chem. C.*, 111:14925-14931, 2007.

[15] Ren, K., Rao, F., Song, Z., Lv, S., Cheng, Y., Wu, L., Peng, C., Zhou, X., Xia, M., Liu, B., and Feng, S. Pseudobinary Al_2Te_3-Sb_2Te_3 material for high-speed phase change memory application. *Appl. Phys. Lett.*, 100: 052105, 2012.